RESEARCH

Experimental investigation on the pore structure and Water Inrush Evolution Law of weakly cemented fault fracture zone with different filling gradations

Yufan Wu · Zhen Huang · Qixiong Gu · Yuansheng Lin · Dickson Moyo · Yun Wu · Chunjiang Zou · Kui Zhao

Abstract   Water and mud inrush caused by fault is a geological disaster characterized by high frequency and huge destructiveness. It is important to study the evolutionary laws of water inrush in fault fracture zones with various filling types. The effect of filling gradation on the mesoscopic structure and seepage characteristics of fault fracture zones was investigated. The law of water inrush evolution and water inrush characteristics of fault-fractured zones with different filling gradations and strong zoning filling characteristics were studied. The results showed that for the larger Talbot gradation indices, the mass of water inrush and the fractal dimension of the lost particles were larger, the peak water pressure and the mass of the lost particles were smaller, and the duration of the initial impermeability stage was shorter for the same loading water pressure. For the fault fracture zones with strong zoning filling characteristics, the peak water pressure, the mass of water surges, and the mass of lost particles were larger, the fractal dimension of the lost particles was smaller, and the duration of the initial impermeability stage was shorter for the fracture zones with larger filling gradation were used as the initial impermeability zones. Furthermore, with larger filling gradation, we observed a greater proportion of large pores, a larger equivalent throat radius, higher pore connectivity, and coordination numbers. Filling gradation and confining pressure greatly affected the permeability of the fault. The permeability decreased by 98.71% when the Talbot gradation indices decreased from 1.25 to 0.6, and decreased by 58.4% when the confining pressure increased from 5 MPa to 15 MPa.

Article highlights

- The influences of filling gradation and zoning filling characteristics on water inrush through the fault fracture zones were revealed.
- The impermeability and water inrush destruction characteristics of fault fracture zones under pressures were investigated.

Y. Wu · Z. Huang · Q. Gu · Y. Lin · D. Moyo · K. Zhao
School of Resources and Environment Engineering,
Jiangxi University of Science and Technology,
Ganzhou 341000, China

Y. Wu · Z. Huang (✉) · Q. Gu · Y. Lin · D. Moyo ·
K. Zhao
Key Laboratory of Mining Engineering of Jiangxi
Province, Jiangxi University of Science and Technology,
Ganzhou 341000, China
e-mail: zhenhuang89@126.com

Y. Wu
State Key Laboratory of Coal Resources and Safe
Mining, School of Mines, China University of Mining &
Technology, Xuzhou 221116, Jiangsu, China

C. Zou
Department of Civil Engineering, Monash University,
Melbourne, Australia

• The mesostructure and seepage characteristics of faults with different filling gradation were investigated.

1 Introduction

The rapid development of the economy and society has led to significant progress in underground engineering in China and other countries (Wang 2003). A series of disasters and accidents may occur during the construction and operation of underground projects, with water and mud inrush induced by fault fracture zones being one of the most typical geological disasters.

The interaction of the underground confined aquifer and construction disturbance causes the filling particles of the broken rock mass to migrate with the water flow, resulting in the continuous expansion of seepage channels, which is a typical fluid-solid coupling (FSC) problem (Wang et al. 2022). Experiments based on the principle of FSC offer notable advantages and find wide applications in solving complex engineering problems. These experiments allow for the consideration of the influence of various operation conditions, factors, and surroundings on the entire process of disasters' evolution, with the added benefit of test repeatability. Zhou et al. (2015) employed diverse regulators for independent adjustments of each index, thereby enhancing material similarity and enabling effective simulation of rock masses and fracture zones with medium and low strength. Based on the FSC theory, Huang et al. (2018) optimized the ratio of FSC materials using orthogonal experiments, resulting in FSC materials meeting the requirements of hydrophilicity, porosity, permeability, and softening coefficient. Hu et al. (2007) utilized gravel, talcum powder, calcite, cement, and gypsum to simulate weak water barriers, yielding positive results in large-scale FSC experiments. In order to investigate the changing laws of mechanical properties, seepage properties, erosion properties, and damage characteristics of broken rock mass during the evolution of water inrush disasters, numerous domestic and foreign experts and scholars carried out a large number of physical model tests. Li et al. (2013) studied the changing law of the displacement field and seepage field of the surrounding rock during the evolution of water inrush under construction disturbance based on a simulation test system for visual observation of the coupled water-rock-flow-solid process. Zhang et al. (2020) simulated water-surge disasters in fault fracture zones with different filling media through experiments, and the results showed that the continuous migration of fine particles changed the flow state of water from laminar to turbulent, which ultimately induced water and mud inrush disasters. Ma et al. (2017) studied the migration laws of fine particles in granular sandstone samples under varying initial porosity, particle size distribution, and seepage pressure through experiments. The results indicate that the migration of fine particles significantly influences the increase in permeability and porosity of the sample during the water inrush process. Zhang (2014) designed a fault water inrush model device and investigated the start-up migration, mutation, and stable evolution of particles during the water inrush process under varying conditions of water pressures, fault widths, and media compositions. Huang (2016) conducted a physical model test of surrounding rock seepage failure and studied the influence of excavation disturbance and the thickness of the anti-outburst layer on the seepage characteristics of the surrounding rock. The results revealed that the hydraulic gradient and permeability of the surrounding rock displayed notable segmental characteristics as the thickness of the outburst prevention layer decreased. Wu et al. (2022a) proposed the use of vertical guide holes as an effective measure to prevent water inrush based on the findings of three-dimensional simulation tests.

The water inrush evolution in fault fracture zones is influenced by pore structures and seepage characteristics. Different pores exhibit varying fluid diffusion and seepage capacities, with mesopores and macropores serving as the primary transport channels for diffusion and seepage (Cai et al. 2013; Zhang et al. 2013). The pore structure model reconstructed by CT scanning truly reproduces the pore structure characteristics of rock (Wang 2014). In recent years, numerous scholars at home and abroad have studied the internal structure of geotechnical materials based on 3D CT reconstruction. Correct segmentation of digital images is essential for CT reconstruction (Liu

et al. 2020), Ramesh et al. (2022) proposed a new image segmentation method that accurately separates soil particles from pores and gives the complete range of pore sizes for different pores. Yu et al. (2023) conducted a quantitative evaluation of the 3D pore-fracture network system in CT slices of volcanic reservoir samples based on Avizo at multiple scales. The results indicates that rock samples with higher diffusion coefficients exhibit higher porosity, more connected pores, larger mean pore volume, and a higher mean coordination number. Luo et al. (2022) investigated the evolution of microstructure and seepage behavior of coal after ScCO2-water treatment based on CT reconstruction technique and computational fluid dynamics, and the results showed that the number of pores and throats of coal after ScCO2-water treatment increased significantly, and the pore connectivity was increased from 44.7 to 67.6%, among which the pores with an equivalent radius of 75 μm contribute the most to permeability. Huang et al. (2021) conducted a comprehensive study on the failure mode of interfacial seepage erosion by CT scanning. The results revealed a three-phase progressive failure during interfacial seepage erosion with increasing hydraulic gradient. The permeability decreases continuously during the process and the failure hydraulic gradient increases with the increase of confining pressure. To gain a better understanding of the seepage characteristics of uranium-bearing sandstone, Sun et al. (2020) combined SEM and CT images to qualitatively analyze the distribution of pores and minerals in the samples. Markussen et al. (2019) analyzed the distribution and connectivity of pores through CT slices to explore the influence of carbonate cementation on porosity and pore throat characteristics. Zhou et al. (2018) extracted the microporous structure model of coal based on Avizo, and numerical simulations were performed on CFX. The results revealed that seepage tends to occur in channels with large pore radii, short paths, and a short distance from the outlet under the condition of low water pressure.

Numerous scholars have simulated the evolution of fault water inrush disasters through physical model experiments, which yielded remarkable outcomes. However, the internal structure of faults is exceedingly intricate, with complex material composition and anisotropy. In this study, a constant pressure erosion water inrush test system is designed and manufactured independently. Based on the FSC method,

the evolution process of water inrush in the fault fracture zone with different Talbot gradation indices (TGI) and strong zonal filling characteristics under different (LWP) loading water pressure was investigated. Additionally, the time-varying laws of water pressure, flow rate, and water inrush quality during the water inrush process were analyzed. Furthermore, the impact of different TGI on the pore structure was analyzed by 3D reconstruction technology. The influential mechanisms of different filling gradation and zonal filling characteristics on the evolution of water inrush in fault fracture zones are revealed at both macroscopic and mesoscopic levels.

2 Experimental materials and methods

2.1 Rock sample of fault

In this paper, the sampling site of the fault fracture zone is Jining, Shandong Province, as shown in Fig. 1. The exposed surface of the fault reveals that the fracture zone mainly consists of mudstone with poor cementation. The faults exhibit significant fragmentation and high density, but low permeability and water content.

The hydraulic properties of the fault fracture zone are significantly influenced by its mineral composition. In this paper, the samples were divided into five groups according to particle size, and the mineral composition of the samples was analyzed using XRD techniques. The results of the X-ray diffraction analysis are shown in Fig. 2, revealing that quartz and kaolinite are the predominant components of the fault fracture zone.
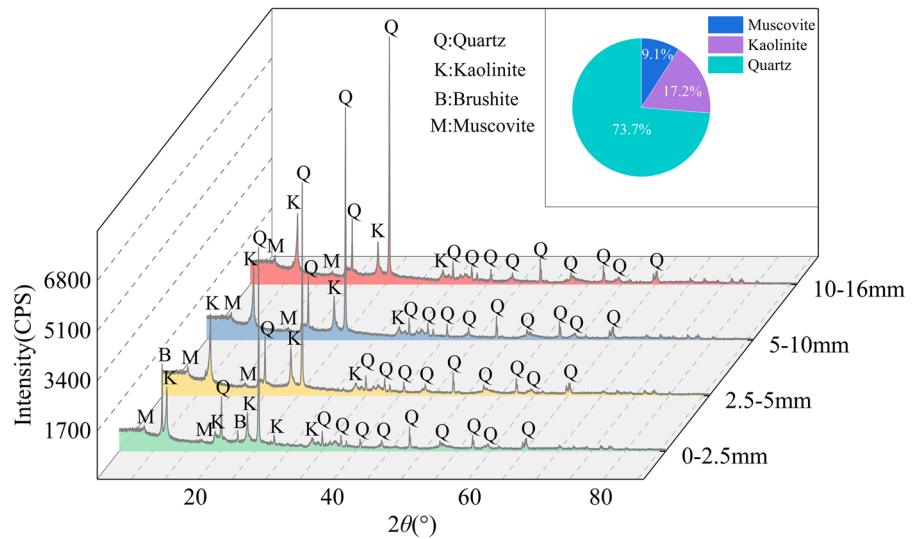
2.2 FSC materials

This paper conducts experiments using FSC materials. Previous researchers have yielded numerous fruitful results in the investigation of FSC materials. Based on previous research and a large number of pre-experiments, we finally chose gravel and sand as the aggregate of the FSC material, gypsum and cement as the cement, and red soil as the regulator. The material ratios are shown in Table 1. The materials are shown in Fig. 3.

The particle size distribution in fault fracture zones exhibits continuity and statistical
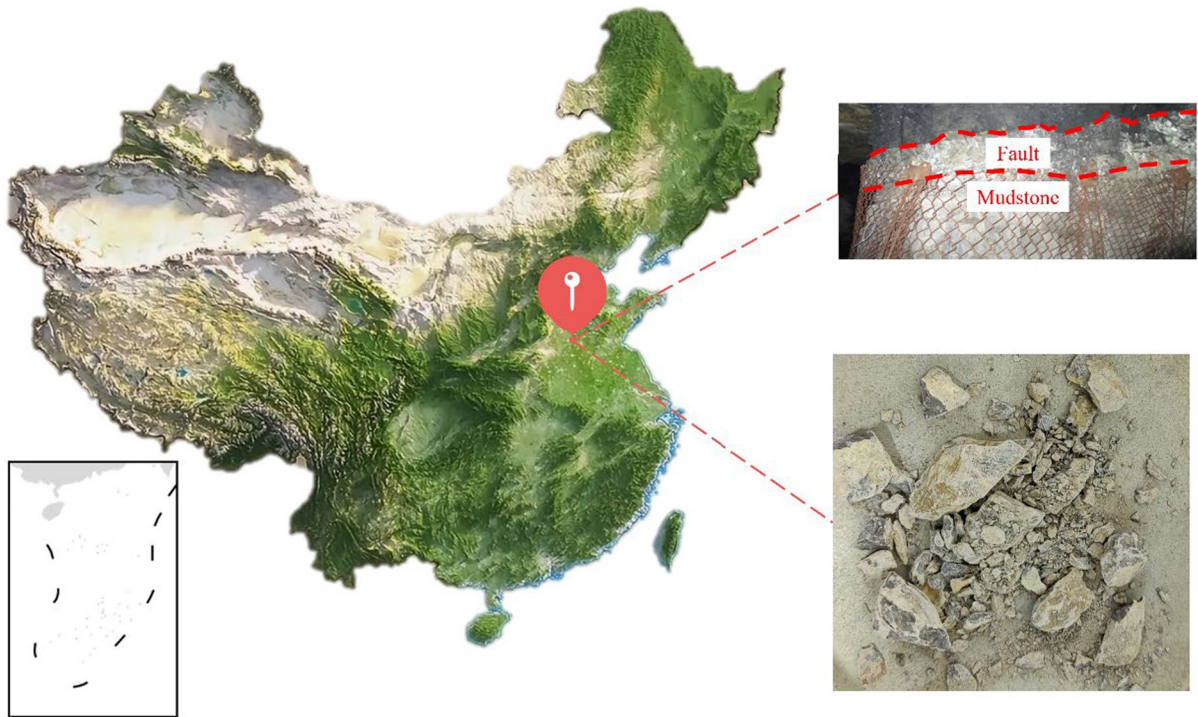
Fig. 1 Samples and sampling sites

Fig. 2 X-ray diffraction

Table 1 Ratio of FSC material

Aggregate cement ratio	Aggregate soil ratio	Cement water ratio
1:0.2	1:0.15	1:0.1

self-similarity, which enables the fractal dimension to be used to quantitatively characterize the particle size gradation distribution of the filling medium in fault fracture zones (Xie et al. 2003; Yu et al. 2021). Based on the fractal theory model proposed by
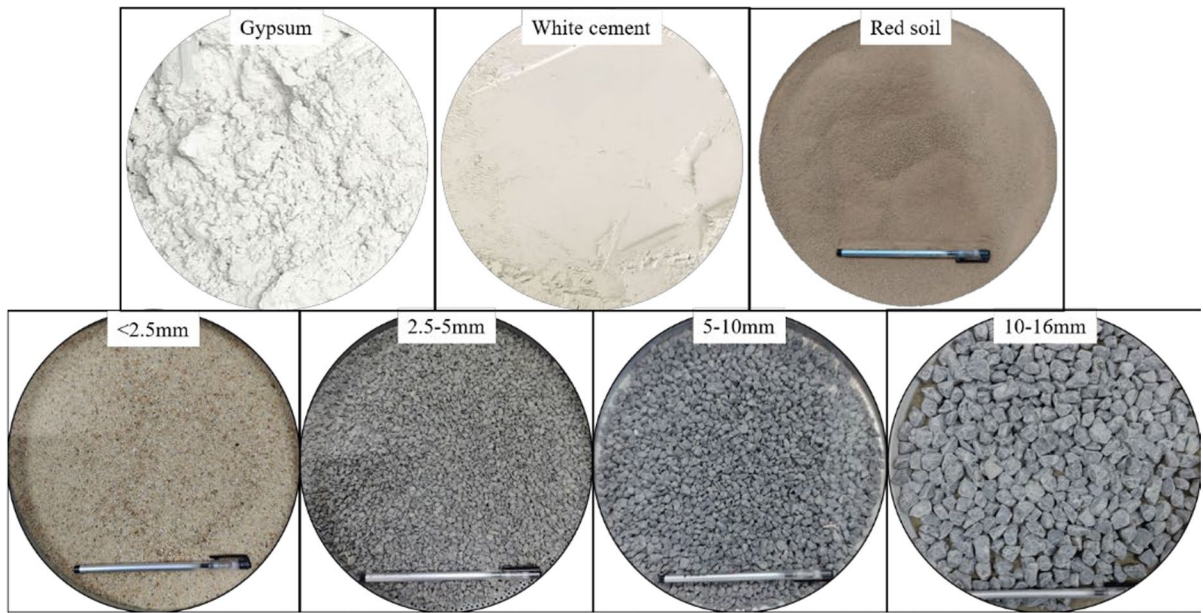
Fig. 3 Materials

Turcotte (Zhang et al. 2022a), the filling particles in the fault fracture zone satisfy Eq. 1:

$$N(\geqslant d) = \frac{k}{d^{D_f}} \tag{1}$$

where d is the particle size, m; N is the number of particles with a size larger than d; D_f is the fractal dimension; and k is a constant.

From Eq. 1, the following relationship exists between the particle mass and the number of particles:

$$\frac{M(d_i)}{M(d_{max})} = \left(\frac{d_i}{d_{max}}\right)^{3-D_f} \tag{2}$$

Take the logarithm of both ends:

$$\lg \frac{M(d_i)}{M} = (3 - D_f) \lg \frac{d_i}{d_{max}} \tag{3}$$

where $M(d_i)$ is the mass of particles with particle size less than d_i; M is the total mass of particles; d_i is the maximum particle size in group I; d_{max} is the maximum particle size.

Therefore, the particle gradation represented in terms of fractal dimension can be expressed as:

$$P_0(d < d_i) = \left(\frac{d_i}{d_{max}}\right)^{3-D_f} \times 100\% \tag{4}$$

where $P_0(d < d_i)$ is the proportion of particles with a size smaller d_i? Replacing $3 - D_f$ with n, Eq. 4 becomes the Talbot grading theory model (Zhu et al. 2011; Yin et al. 2020).

$$P_0(d < d_i) = \left(\frac{d_i}{d_{max}}\right)^{n} \times 100\% \tag{5}$$

In this study, the power exponent 'n' of the Talbot function is used to quantitatively characterize the filling particle size distribution of the fault fracture zone. The n-value of the fault-fracture zone rock sample calculated from Eq. 5 is 1.04. Based on the characteristics of fault fragmentation zones and previous studies (Li 2018; Wu 2019a; Zhang et al. 2019; Huang et al. 2022), the TGI chosen for this paper are 1.25, 0.85, 0.65, 0.5, and 0.35. The proportion of aggregate with different sizes for different TGI is shown in Table 2.

Table 2 Proportion of different particle size aggregates with different TGI

TGI	$P_0(d < d_i)$ (%)			
	2.5 mm	5 mm	10 mm	16 mm
0.35	52.22	66.56	84.43	100
0.50	39.53	55.90	79.06	100
0.65	29.92	46.95	73.68	100
0.85	20.64	37.21	67.07	100
1.25	09.82	23.36	55.57	100

2.3 Test programs

2.3.1 NMR tests

FSC material is a porous medium composed of aggregate and cement. FSC materials with different TGI exhibit different pore structures due to the irregular shape of aggregate particles and proportional differences of particles with different sizes. The hydraulic properties of geotechnical materials are closely related to the pore structure. Nuclear Magnetic Resonance (NMR) technology is a fast, efficient, and non-destructive detection method for characterizing pore, fissure, and pore size distribution in the field of geotechnical engineering (Heidary 2021; Wu et al. 2022b). In this paper, the NMR technique is used to study the porosity of FSC materials with different TGI. The test equipment is the PQ-001 (Mini-NMR). The test process is shown in Fig. 4: (1) The raw materials were weighed and made into specimens of 50 mm diameter and 100 mm height. (2) The specimens were kept in a constant temperature and humidity curing box for three days and then saturated with a vacuum saturator. (3) The mould is removed after

the specimen is saturated, and then the specimen is placed in the NMR instrument to measure the porosity. Considering the special properties of FSC materials, the following two points should be paid attention to during the test: Firstly, to reduce the dispersion of the aggregate distribution, a layered sampling method was employed, where a specimen was paved five times, each with a pavement height of 2 cm. Secondly, to maintain specimen integrity, the mould was not demoulded during curing and vacuum saturation.

2.3.2 CT tomography tests

Structural characteristics such as distribution, connectivity, shape, and size of pores in geotechnical materials plays a decisive role in water seepage (Wu 2019a; Li et al. 2019; Scibek et al. 2021). X-ray imaging is a non-destructive analysis technique that has been widely applied, and it can accurately, quickly, and effectively analyze the fine structure of pores and cracks within the geotechnical material. For this study, the equipment used is the nano Voxel-3502E 3D x-ray imaging system manufactured by Sanying China, as shown in Fig. 5.

In this paper, specimens with TGI of 0.35, 0.65, and 1.25 were subjected to CT tomography, and the 3D visualization software Avizo was used for 3D reconstruction analysis. The results of the Avizo visualized 3D reconstruction are shown in Fig. 6. Firstly, CT slices were imported into Avizo for pre-processing. Noise reduction and brightness averaging were conducted using the Non-Local Means Filter algorithm and the Beam Hardening Correction algorithm, respectively, as shown in Fig. 6a. The Non-Local Means Filter algorithm is implemented based on the adaptive-manifolds method (Gastal and Oliveira

Fig. 4 The procedure of the NMR test
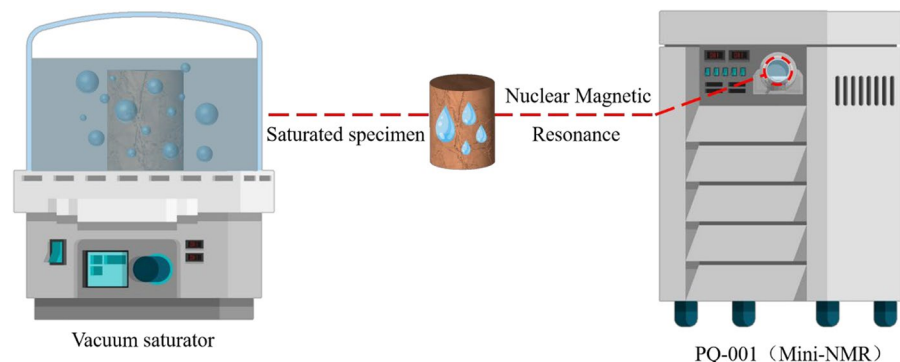
Fig. 5 Nano Voxel-3502E 3D x-ray imaging system
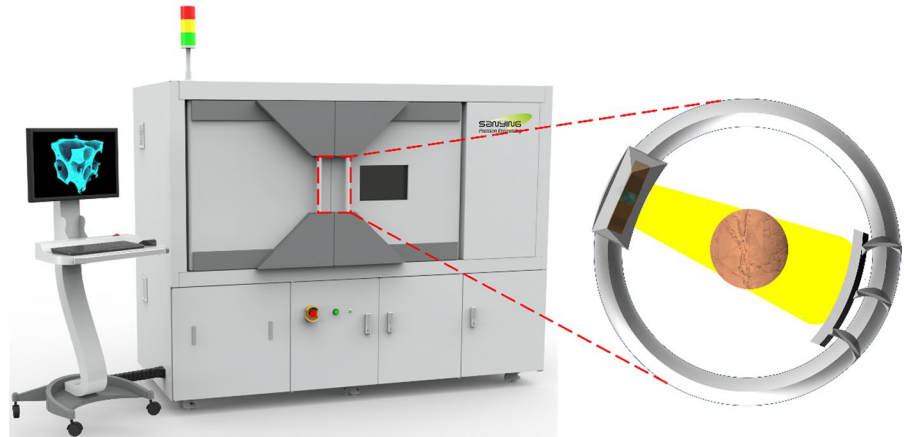
2012), and the Beam Hardening Correction algorithm is implemented by calculating the mean radial intensity profile first and then smoothing it using Gaussian filters. After the preprocessing of the data was completed, Watershed Segmentation was used to segment the large pores, and Top-Hat Segmentation was used to segment the micro pores. All the pores of the specimen were obtained by adding the two segmentation results, as shown in Fig. 6c. Errors caused by human operation can be minimized by combining Watershed Segmentation and Top-Hat Segmentation. The Watershed Segmentation performs an accurate segmentation of different phases by applying a watershed on the high gradient magnitude. The Top-Hat segmentation extracts small elements and details from given images. It detects the dark or the white area, corresponding to the valleys or the narrow peaks. The type of pore is critical to the seepage characteristics of geotechnical materials (Iarje et al. 2023), where macropores can greatly improve the permeability of geotechnical materials, and the equivalent radius of pores extracted with Avizo is greater than 1000 μm as shown in Fig. 6d. The Axis Connectivity algorithm was used to extract connectivity pores and analyze the connectivity of the pores. Given two parallel planes and a binary (or label) input image, the Axis Connectivity algorithm generates a binary image containing all paths connecting the two planes. Finally, the Separate Objects Module and the Generate Pore Network Model were applied to display the connection of pores and throats and analyze the distribution characteristics of pores, as shown in Fig. 6e. The Separate Objects Module is a high-level combination of

watershed, distance transform, and numerical reconstruction algorithms.

2.3.3 Triaxial permeability test

The permeability is an important indicator of the hydraulic properties of geotechnical materials. In this paper, the permeability of FSC materials with different TGI under different confining pressures is investigated based on the Top-Rock multi-field coupled triaxial test system. The test system is shown in Fig. 7. In addition, the permeability of FSC materials without confining pressure was calculated based on CT reconstruction. The following is the general process of the triaxial permeability test. After installing the specimen, the confining pressure was loaded to 5 MPa. 3 MPa of osmotic pressure was applied upstream of the specimen, and when the osmotic pressure downstream began to increase, 1 MPa of osmotic pressure was applied downstream of the specimen. Start the test after the upstream and downstream pressure has stabilized, and the test time is 5–10 min. After the end of the test with a confining pressure of 5 MPa, the confining pressure was sequentially increased to 10 MPa and 15 MPa. The test time at the confining pressures of 10 MPa and 15 MPa was also 5–10 min.

2.3.4 Water inrush tests

The test system comprises a pressurization control module, a pressurized water inrush module, and a data acquisition module. The pressurization control module includes a constant pressurization pump, a non-negative pressure stabilizing tank, a pressure
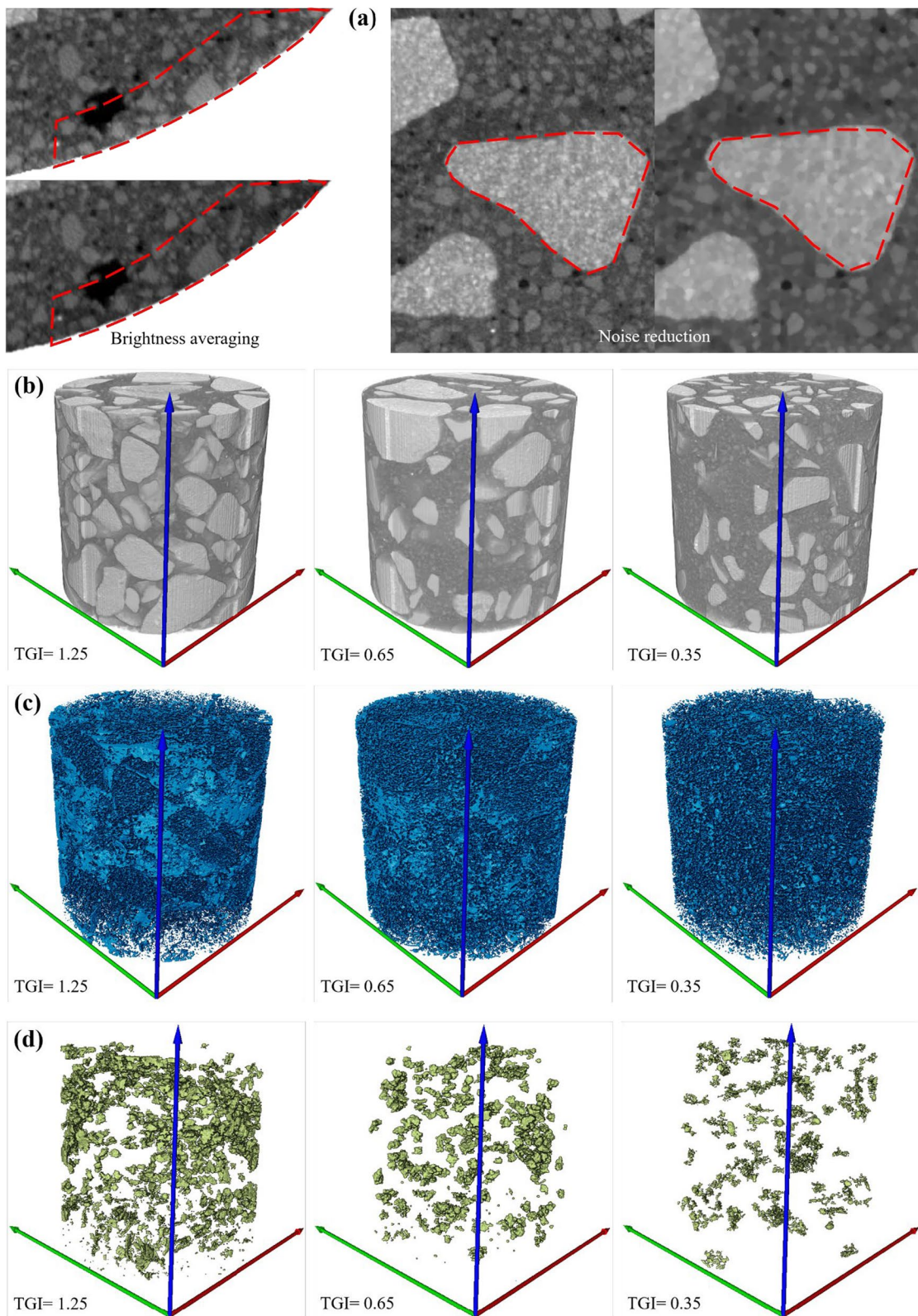
Fig. 6 Avizo visualizes 3D reconstruction results. **a** Images preprocessing, **b** reconstructed specimens, **c** all pores, **d** pores of size over 1000 μm, **e** pore network modeling
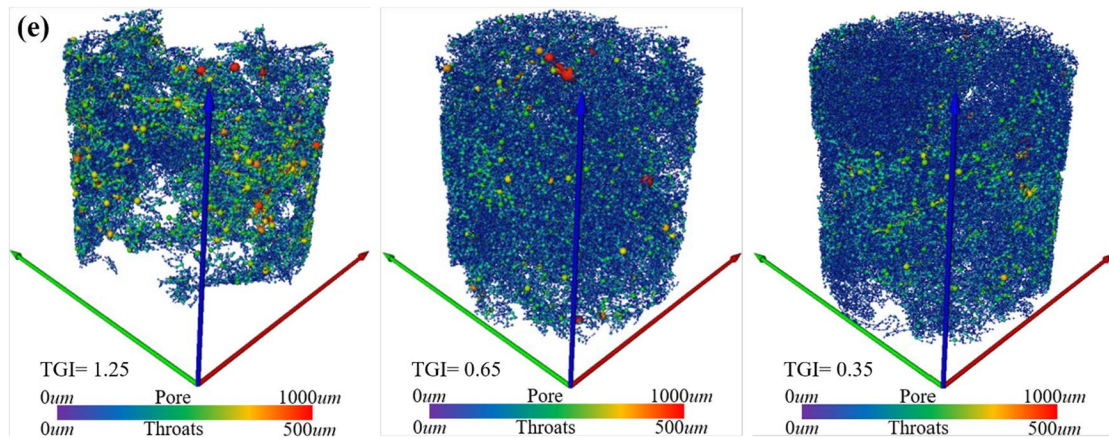
Fig. 6 (continued)

Fig. 7 Top-Rock multi-field coupled triaxial test system

gauge, a precision flow control valve, and high-pressure pipes. The maximum LWP that the test system can withstand is 22,000 kPa considering the safety, the maximum LWP of experiments is set to 900KPa. The pressurized water inrush module comprises a filling cavity and a sealing part. The filling cavity is manufactured by 3D printing technology, while the sealing part is a high-strength aluminum alloy module machined by computer numerical control. In order to minimize the influence of the size effect (Zhang et al. 2022b), we designed the inner diameter of the filling cavity to be 5 times the maximum diameter of the

FSC material rock (Xie et al. 2015; Wu et al. 2018), i.e., 75 mm, while the height was 130 mm. The filling cavity is equipped with three water pressure monitoring points, No. 1, No. 2, and No. 3, which are evenly distributed along the axial direction. The data acquisition module includes pressure transmitters, a micro flow meter, a paperless recorder, an HD camera, an electronic scale, and beakers. First, we use the layered sampling method to prepare samples in the filling cavity. After the sample preparation was completed, the pressurized water inrush module was assembled and left to stand for 30 min. During this standing period,

Fig. 8 Schematic diagram of the water inrush test system
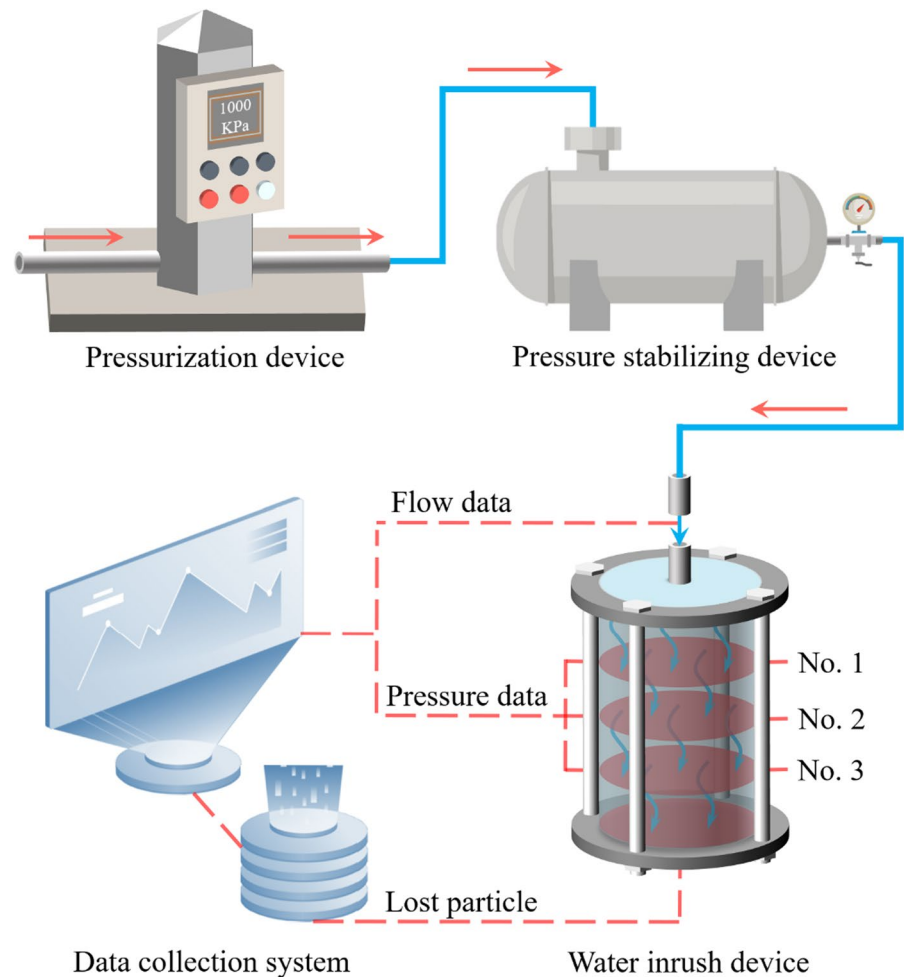
the pressurized control module and data acquisition module were activated to calibrate the equipment, and the flow rate was set to 15 l/min. The pressurization control module and pressurized water inrush module were connected after the sample was left to stand for 30 min. Meanwhile, the moments of the beginning and end of the experiment were recorded. The experimental process is shown in Fig. 8.

The tests were grouped based on different TGI and LWP, as shown in Table 3. The TGI for FSC materials of test numbers 1–9 are single, while the FSC materials of test numbers 10–15 were layered. The filling cavity was divided evenly into two layers along the axial direction, designating the layer near the water inlet as the U layer and the layer near the water outlet as the S layer, as shown in Fig. 9. The TGI of the U-layer FSC material of test numbers 10 to 12 is 1.25, while the TGI

of the S-layer FSC material is 0.35. Conversely, the TGI of the U-layer FSC material of test numbers 13 to 15 is 0.35, while the TGI of the S-layer FSC material is 1.25.

3 Results and discussion

3.1 Analysis of NMR tests

The changing trend of porosity with TGI is shown in Fig. 10. The porosity is directly proportional to the TGI, as can be concluded from the figure. The larger the TGI, the larger the porosity of the specimen. An increase in the proportion of fine particles will reduce the porosity of the specimen. This is attributed to the
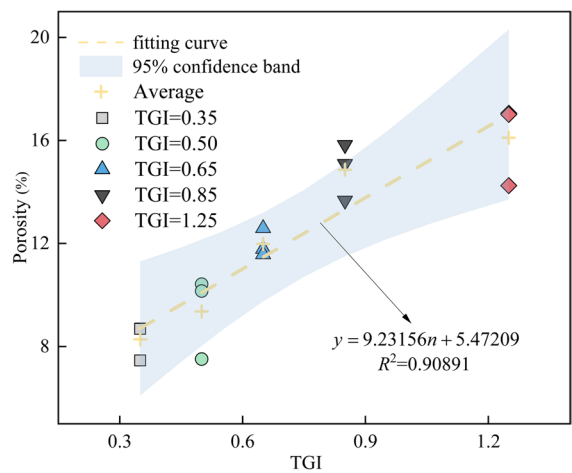
Fig. 9 Schematic diagram of the layered FSC material
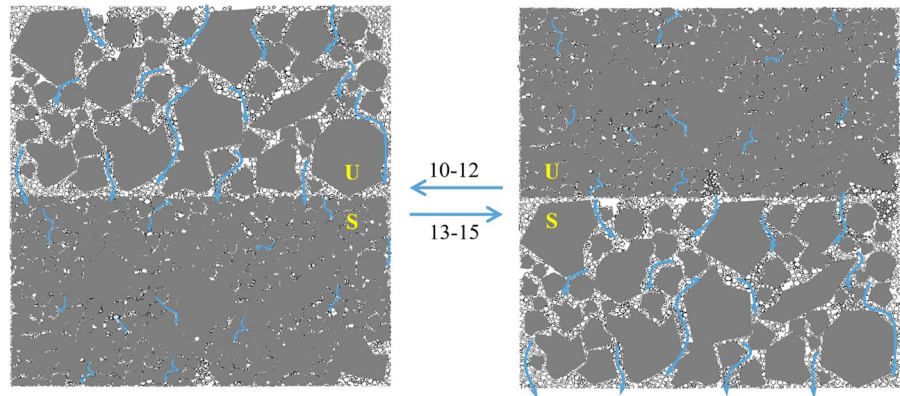
Table 3 Water inrush design of experiments

Test No.	TGI	LWP (KPa)
1	1.25	300
2	0.65	300
3	0.35	300
4	1.25	500
5	0.65	500
6	0.35	500
7	1.25	700
8	0.65	700
9	0.35	700
10	U = 1.25 & S = 0.35	500
11	U = 1.25 & S = 0.35	700
12	U = 1.25 & S = 0.35	900
13	U = 0.35 & S = 1.25	500
14	U = 0.35 & S = 1.25	700
15	U = 0.35 & S = 1.25	900

$$y = 9.23156n + 5.47209$$
$$R^2 = 0.90891$$

Fig. 10 The porosity of specimens with different TGI obtained from NMR tests

irregular shape of skeleton particles, making complete gap-filling challenging. At the same time, the fine particles have strong fluidity and certain plasticity during sample preparation, which can fill the gaps between the skeleton particles. More gaps are filled when the number of fine particles is sufficient, which results in a lower porosity of the sample. The increase in fine particles was 42.4%, while the porosity decreased by 48.57% when the TGI of the FSC material decreased from 1.25 to 0.35. We performed a linear fit between TGI and average porosity, resulting in $R^2 = 0.90891$, which indicates a large correlation between TGI and porosity.

3.2 Analysis of CT reconstruction

The porosity and pore connectivity of specimens with different TGI are shown in Fig. 11. Among them, the porosity of samples with different TGI is shown in Fig. 11a. Plane porosity is the proportion of the area of pores in each slice, which represents the distribution of pores along the specimen's axial direction. There are a larger number and value of peaks in the plane porosity curves of the specimens with TGI of 1.25 and 0.65, which suggests that the specimens with lower TGI possess a more uniform pore distribution. It is caused by the fact that the macroporous proportion decreases as the TGI decreases. The trend of porosity variation obtained through CT reconstruction is consistent with the experimental results

Fig. 11 Porosity and the connectivity of pores obtained by CT reconstruction. **a** The porosity of the plane and porosity of specimens, and **b** the connectivity of pores
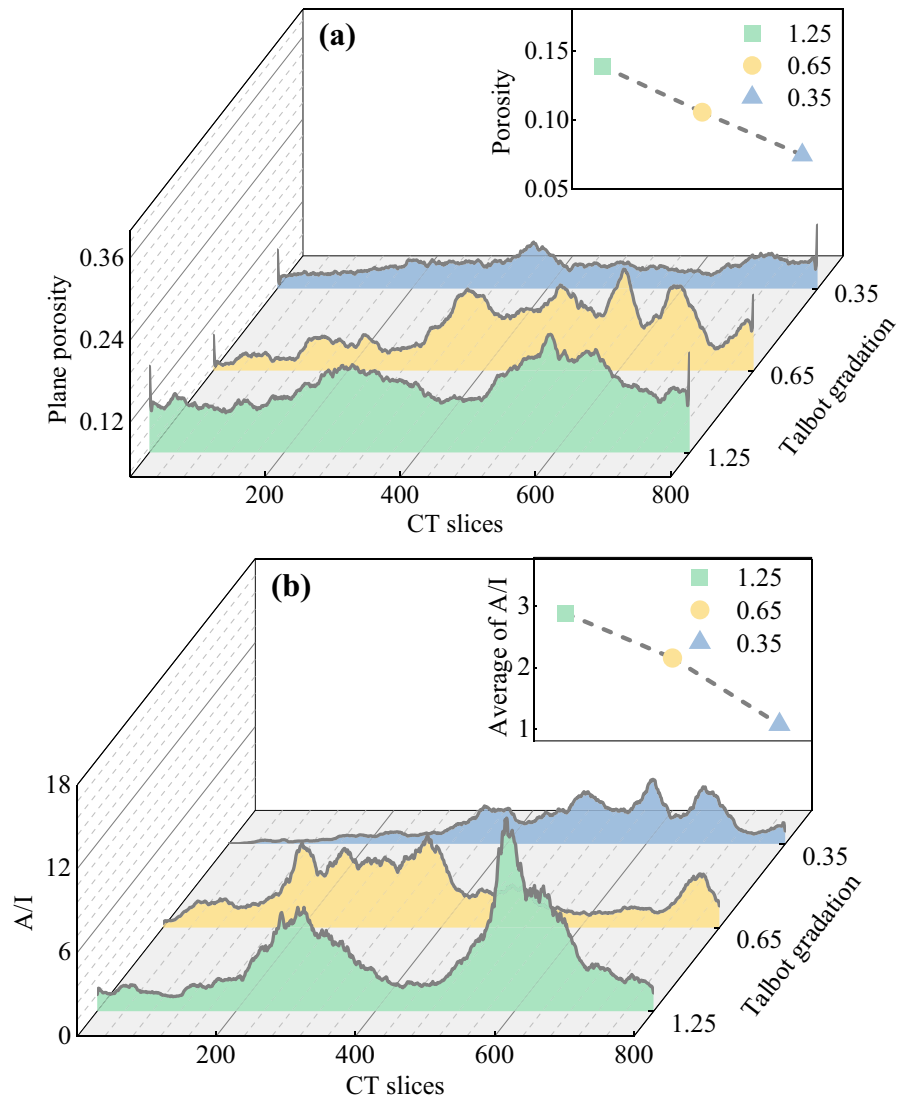

from NMR analysis. In this paper, A/I (the ratio of the volume of connected pores to that of isolated pores) is used to represent the connectivity of pores. The connectivity of the pores of the specimens with different TGI is shown in Fig. 11b. Pore connectivity exhibits a directly proportional relationship with TGI. The distribution curves of pore connectivity along the axial direction exhibit a multi-peak pattern, with local peaks diminishing as the TGI decreases. The effect of the TGI of the specimens on pore connectivity was significant. As the TGI decreased from 1.25 to 0.35, the connectivity of the pores decreased by 62.85% from 2.88 to 1.07. This outcome arises due to the higher proportion of fine particles associated

with smaller TGI values. This is because the number of fine particles in the specimen is more sufficient at smaller TGI, and more of the skeleton gaps will be filled. The result is a reduction in the proportion of macropores and the porosity of the specimen, thus resulting in lower connectivity of pores.

The coordination number and throat equivalent radius of specimens with different TGI are shown in Fig. 12. The distribution of coordination number is shown in Fig. 12a. The coordination number represents the count of throats connected by an individual pore. Greater coordination numbers indicate improved pore connectivity and a greater number of channels for fluid migration (Fan et al. 2020). This
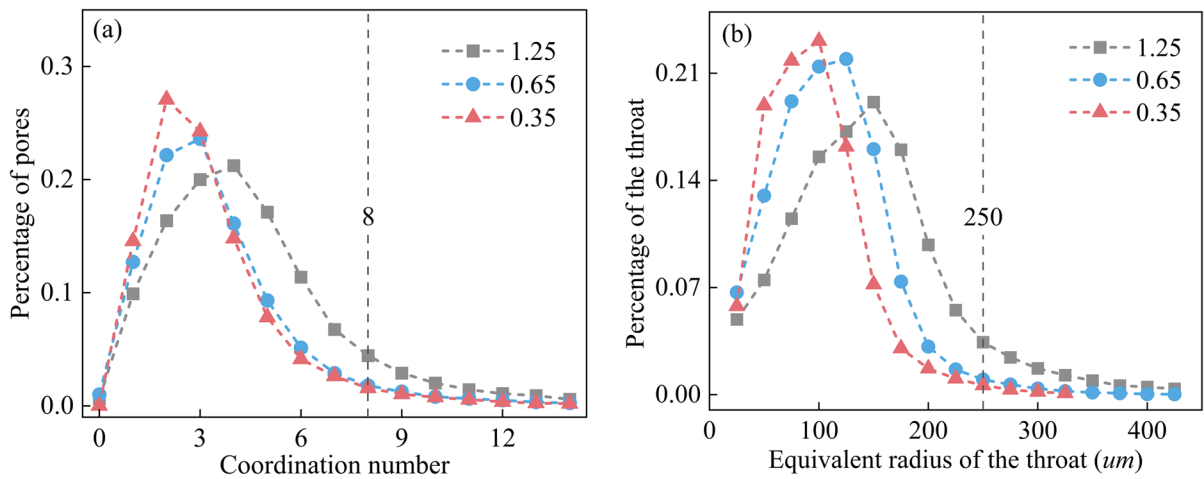
Fig. 12 The coordination number and throat equivalent radius for different TGI. **a** The distribution curve of coordination number, **b** the distribution curve of the equivalent radius of the throat

means that the coordination number of isolated pores is 0. The distribution curves of the coordination number are unimodal. As the TGI of the specimens increases, the curve's peak point gradually shifts toward the lower right. The peak coordination numbers were 2, 3, and 4 for specimens with TGI of 0.35, 0.65, and 1.25, respectively. Additionally, the proportion of pores with coordination numbers less than 8 was 89.85%, 93.95%, and 95.28% for specimens with TGI of 0.35, 0.65, and 1.25, respectively. The larger the TGI, the larger the mean of the coordination number. This indicates that the channels for fluid flow increase with increasing TGI, which leads to an increase in the connectivity of pores.

The distribution of the equivalent radius of the throat is shown in Fig. 12b. The distribution curves of the equivalent radius of the throat are unimodal, and the peak points shift progressively to the lower right with increasing TGI of the specimens. Peak throat equivalent radius was 100 μm, 125 μm, and 150 μm for specimens with TGI of 0.35, 0.65, and 1.25, respectively. Moreover, the proportions of throats with an equivalent radius less than 250 μm were 91.50%, 98.42%, and 99.26% for specimens with TGI of 0.35, 0.65, and 1.25, respectively. This indicates that the average radius of the gushing channels increases with increasing TGI of the specimen, which leads to increased connectivity of pores.
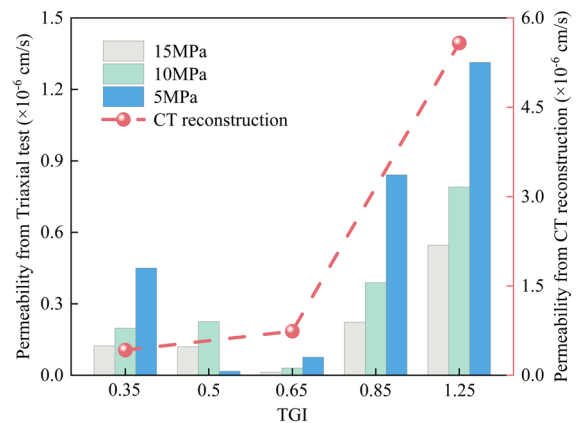
Fig. 13 Permeability of FSC materials

3.3 Analysis of permeability

The permeability of FSC materials at different confining pressures is shown in Fig. 13. Where the permeability from CT reconstruction was calculated based on the Absolute Permeability Experiment Simulation module, which is based on an experimental simulation using the Stokes equation. The simulations show that the permeability monotonically increases with increasing TGI. However, experimental results based on triaxial seepage show that the permeability tends to decrease and then increase with increasing TGI. This discrepancy may stem from two main factors. Firstly, the high confining pressure has redistributed

the skeleton particles inside the specimen, resulting in a change in the internal structure of the material. In particular, specimens with smaller TGI are more lacking in skeletal particles, and the strength of the specimen is lower, which results in more macroscopic fracture under higher confining pressure. This leads to a gradual decrease in permeability as the TGI increases from 0.35 to 0.65. Secondly, the absolute permeability simulation based on Stokes equation assumes the boundary conditions that there is no slip phenomenon at the fluid-particle interface as well as between the planar and pore models and that the pore structure does not change with the duration of the simulation time. However, in the actual test, due to the characteristics of the fluid-solid coupling material, the migration of fine particles during the seepage process caused changes in the pore structure, which affected the results of the permeability. However, the overall trend of the permeability increases with increasing TGI. Confining pressure and permeability are inversely related. This is because the increase in confining pressure leads to the gradual compression of pores and fissures within the specimen, which results in a decrease in permeability. Filling gradation and confining pressure greatly affect the permeability of FSC materials. When the TGI was reduced from 1.25 to 0.65, the permeability of FSC material under 5 MPa confining pressure was sharply reduced from 1.3135×10^{-6} cm s^{-1} to 0.0169×10^{-6} cm s^{-1}, which was reduced by 98.71%. When the confining pressure was increased from 5 MPa to 15 MPa, the permeability of TGI of 1.25 decreased sharply from 1.3135×10^{-6} cm s^{-1} to 0.5464×10^{-6} cm s^{-1}, which was reduced by 58.4%.
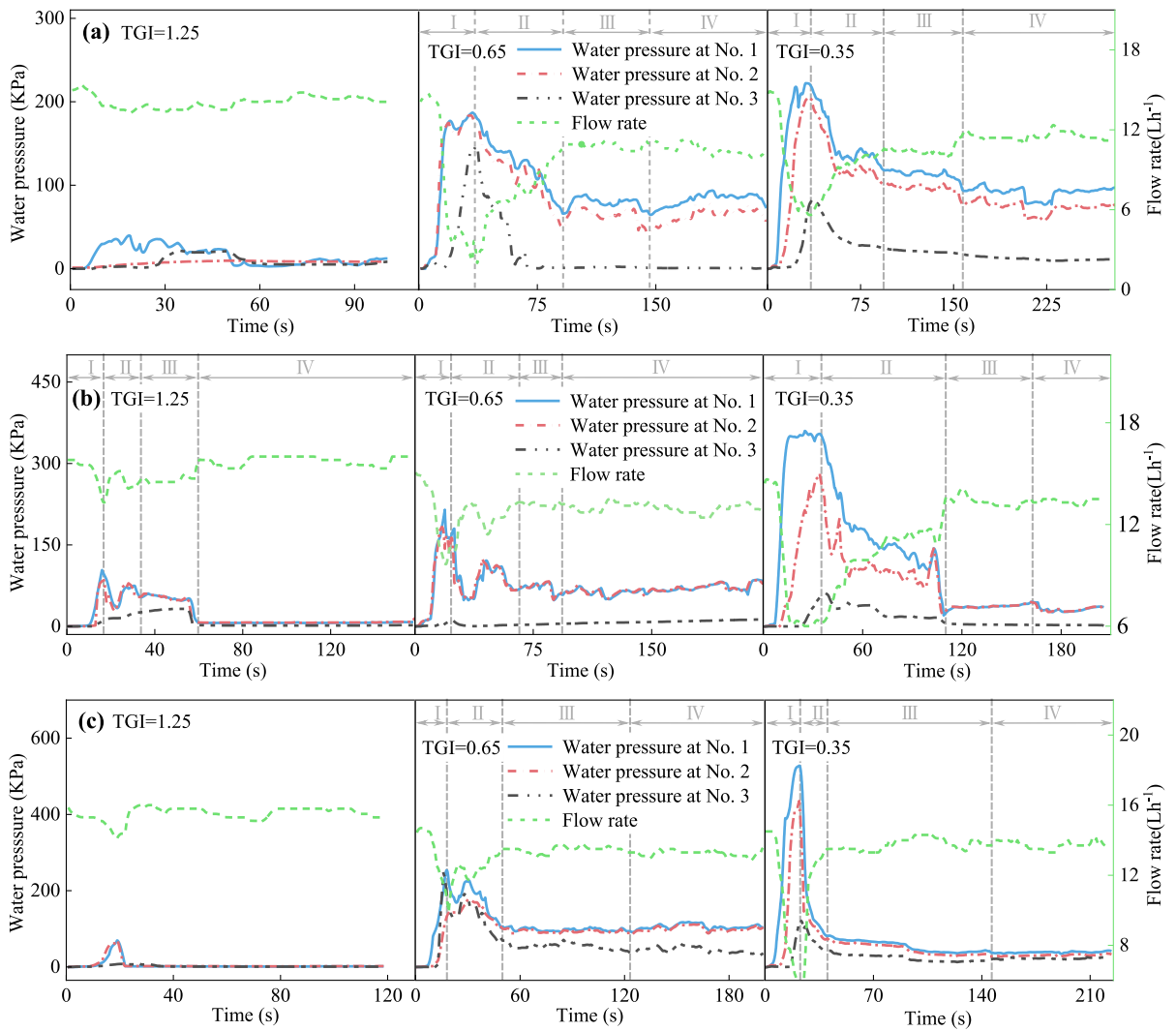
3.4 Analysis of erosion water inrush test

3.4.1 Time-varying evolutionary laws of water pressure and flow rate

The time-varying curves of water pressure and flow rate for FSC materials with different TGI at different LWP are shown in Fig. 14. This figure indicates a significant dispersion in the test results for the FSC material with a TGI of 1.25. This is attributed to the large porosity, high proportion of macropores, and high pore connectivity of the FSC material with a TGI of 1.25. This results in materials that are less impermeable, which enables gushing channels to

develop quickly. The following discussion will focus on the results of tests with TGI of 0.65 and 0.35.

The water inrush process, as inferred from the time-varying curves of water pressure and flow rate, can be divided into four distinct stages: (1) Initial impermeability stage – characterized by the rapid increase of water pressure from 0 to the peak, concomitant with a swift decline in the flow rate and the onset of water seepage. (2) Rapid expansion stage of seepage channels – marked by erosion and damage of the FSC materials by the water flow, with a dramatic decrease in water pressure and a rapid increase in flow rate. (3) Steady expansion stage of gushing channels – during which the flow rate remains relatively constant, but the water pressure gradually diminishes. This is because the fine particles on the seepage sidewalls are continuously eroded away by the water, and the seepage channels are constantly expanding, leading to a gradual decrease in water pressure. (4) Stable stage of water inrush – characterized by a relatively stable flow rate and water pressure, the gushing water changes from turbid to clear, signifying the complete formation of the gushing channel. The evolution process of erosion and water inrush is shown in Fig. 15. The time to reach the peak water pressure at measurement point No. 3 for the FSC materials with TGI of 0.65 was 37s, 25s, and 16s for the LWP of 300KPa, 500Kpa, and 700KPa, respectively, while the time the FSC materials with TGI of 0.35 was 38s, 34s, and 22s, respectively. Under identical LWP, the duration of the initial impermeability stage is inversely proportional to the TGI of FSC material. A smaller TGI of FSC materials corresponds to a more pronounced hysteresis in water pressure transmission, which indicates greater impermeability.
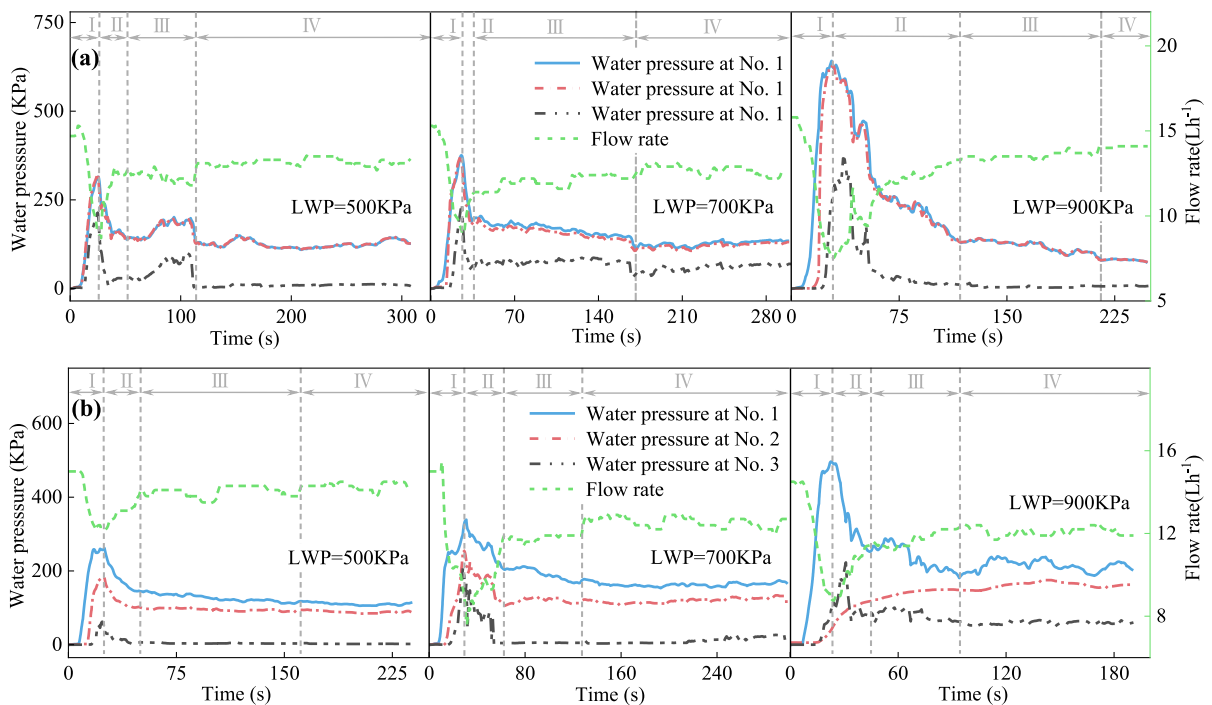
The time-varying curves of water pressure and flow rate of FSC materials with different zonal filling characteristics under different LWP are shown in Fig. 16. Based on the time-varying curves of water pressure and flow rate, the water inrush process within the fault fracture zone with zonal filling characteristics can be divided into four distinct stages: the initial impermeability stage, rapid expansion of seepage channels, steady expansion of gushing channels, and stable stage of water inrush. The trends of water pressure and flow rate in the FSC materials with layered features are consistent with those in the FSC materials with single TGI. The water pressure time-varying curves of No. 1 and No. 2 are consistent

Fig. 14 Time-varying curves of water pressure and flow rate for various TGI under distinct LWP. **a** LWP of 300KPa, **b** LWP of 500KPa, **c** LWP of 700KPa.
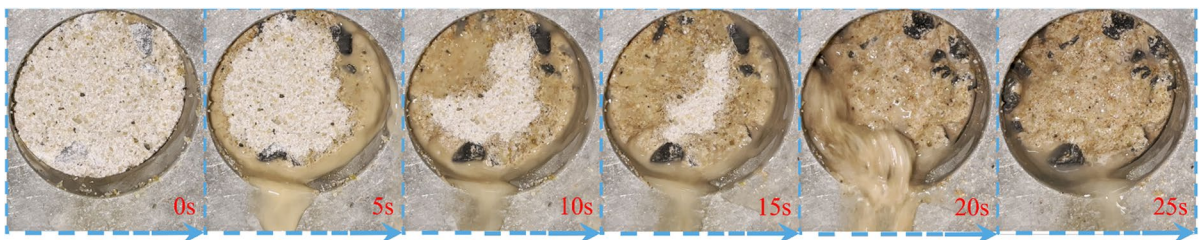
Fig. 15 The evolution process of erosion and water inrush

Fig. 16 Time-varying curves of water pressure and flow rate for varying zonal filling characteristics under distinct LWP. **a** TGI for the U layer is 1.25, TGI for the S layer is 0.35, **b** TGI for the U layer is 0.35, and TGI for the S layer is 1.25

when the U = 1.25. While the water pressure of No. 2 is lower than that of No. 1 at any time when the U = 0.35. This reflects the greater impermeability of materials with a TGI of 0.35. From the curve of water pressure and flow rate, the duration of water and mud inrush is longer at U = 1.25. This is due to the inconsistent migration process of fine particles. At U = 1.25, the seepage channel is blocked when the upstream fine particles migrate to the downstream. Furthermore, the formation of dominant seepage channels took longer due to a more uniform distribution of water pressure downstream.

3.4.2 Time-varying law of the mass of water inrush

Figure 17 illustrates the time-varying curves of water inrush mass in the fault fracture zone with various TGI and zonal filling characteristics under varying LWP. Under the identical LWP, the larger the TGI of the FSC material, the greater the mass of the water inrush. Under the identical TGI of the FSC material, the larger the LWP, the greater the mass of the water inrush. This is because the water pressure and

flow rate output from the test equipment is constant, as the TGI is larger, the porosity and proportion of macropores in the FSC material is larger, and the connectivity of the pores is greater, which results in more gushing channels will be developed during the experiment. With the identical TGI of the FSC material but higher LWP, the water is more erosive, resulting in more particles being lost by erosion. Thus a larger size of the gushing channels is developed. When the FSC material is characterized by layering, a greater mass of water inrush in the FSC material with a TGI of 1.25 for the U-layer under the same LWP. The difference in water inrush mass of the FSC materials with different zonal filling characteristics gradually decreases with the increase of LWP. The mass of the water inrush is almost equal when the LWP is 900 KPa.

3.4.3 Characteristics of erosion and water inrush

The water inrush characteristics for FSC material with different TGI at varying LWP are shown in Fig. 18. The peak water pressure diminishes with rising TGI
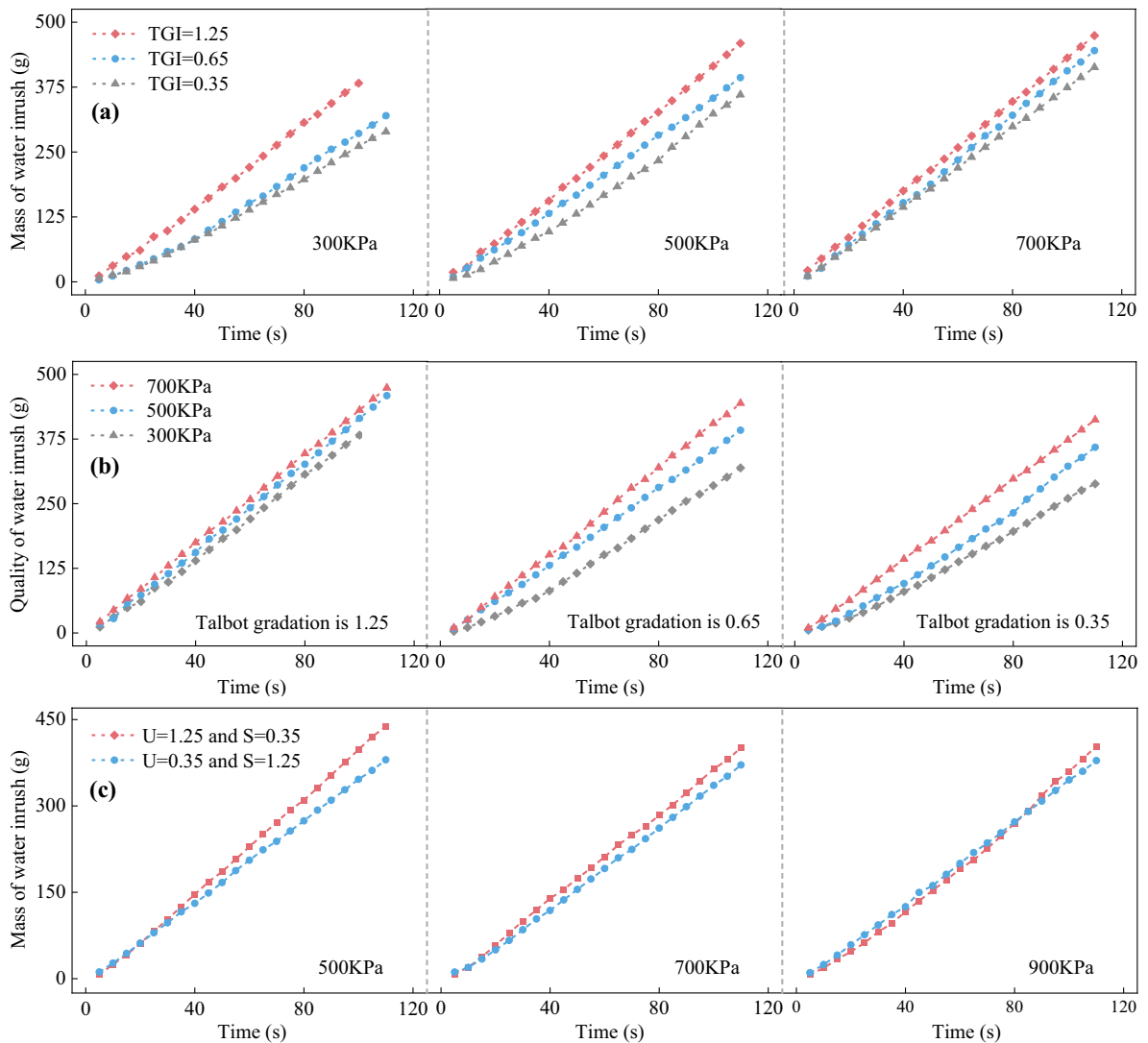
Fig. 17 Time-varying curves of the mass of water inrush. **a** Mass of water inrush for different TGI under the same LWP, **b** mass of water inrush for the same TGI with different LWP, **c** mass of water inrush in fault fracture zone with different zonal filling characteristics under different LWP.

and escalates with augmented LWP. The larger the TGI, the earlier the water inrush occurs under the same LWP. The mass of lost particles decreases with the increase of TGI, and the fractal dimension of lost particles increases with the increase of TGI. The water is more likely to be impeded within the FSC material of smaller TGI due to lower porosity and the impact of migration and blockage of the sand and clay particles. This results in a slower water pressure transfer, which is reflected in the greater time difference for pressure to start appearing at measurement points

1 and 3. Under equivalent LWP, larger water pressure can be accumulated by the FSC materials with smaller TGI before the water inrush, which leads to a greater instantaneous gushing of water and damage. Additionally, this resulted in more skeleton particles and fine particles being carried out by the gushing water. Owing to the hydrophilicity of FSC materials, particles with small geometric sizes are more likely carried out by the gushing water when the cemented part softens and disintegrates, while particles with large sizes cannot follow the water migration due to
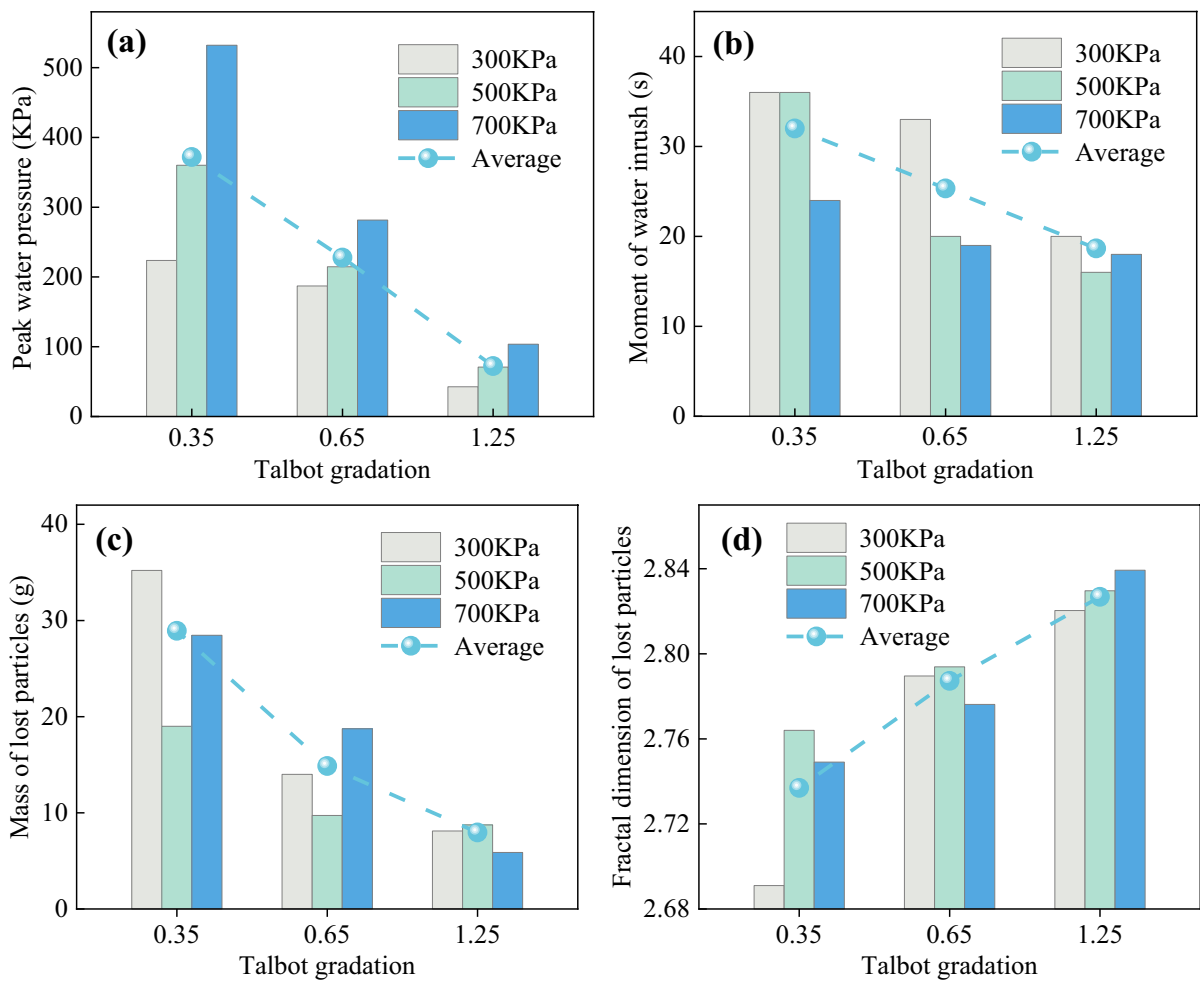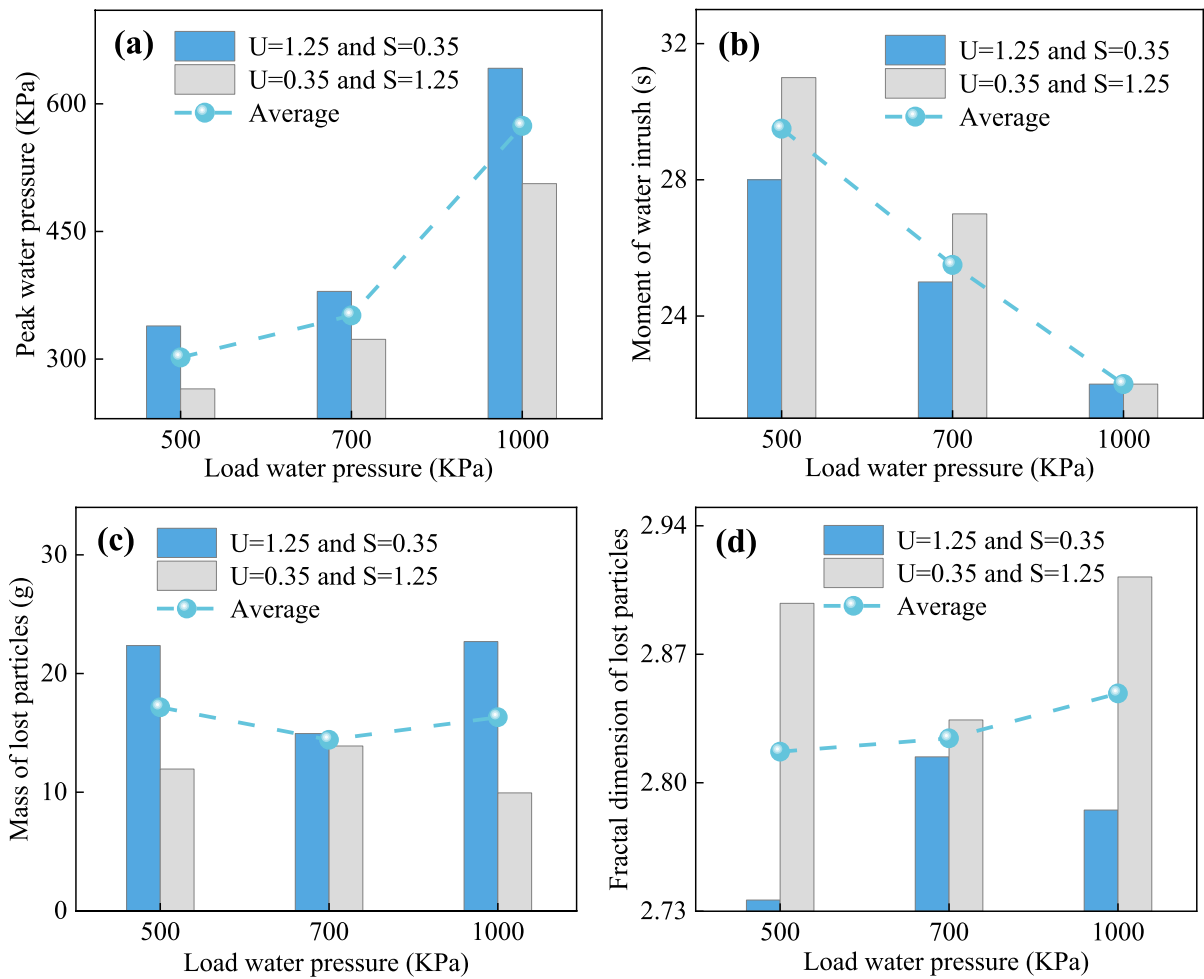
Fig. 18 Water inrush characteristics for FSC material with different TGI at varying LWP. **a** Peak water pressure, **b** moment of water inrush, **c** mass of lost particles, **d** fractal dimension of lost particles

spatial constraints. The higher the proportion of fine particles, the longer it takes for the seepage channels to fully develop, and the impermeability properties persist after the first water inrush, which results in a larger area for water to diffuse within the material, and a higher degree of softening and disintegration of the material. Consequently, the greater the proportion of fine particles in the material, the greater the number of lost particles. In addition, the seepage channel can be fully developed in a shorter period, which leads to a smaller water diffusion area, weaker softening of the FSC material, and fewer skeleton stones being washed out by the water, so the fractal dimension of the lost particles is larger. To sum up, under the same conditions, faults with smaller filling

gradation possess stronger impermeability properties, and the water inrush occurs later, but the amount of water gushing and mud inrush is greater.

The water inrush characteristics of FSC material with diverse zonal filling characteristics under varying LWP are illustrated in Fig. 19. The peak water pressure and mass of lost particles were greater for the experiment with a TGI of 1.25 for the U layer at the same LWP. However, the fractal dimension of the lost particles is smaller, and the moment of water inrush is earlier. With consistent zonal filling characteristics, the peak water pressure escalates with increasing LWP, while the moment of water inrush is delayed. This is because, with a TGI of 1.25 for the FSC material in the U-layer,

Fig. 19 Water inrush characteristics for FSC material with different zonal filling characteristics at varying LWP. **a** Peak water pressure, **b** moment of water inrush, **c** mass of lost particles, **d** fractal dimension of lost particles

the porosity of the upstream FSC material is large, and the upstream fine particles are susceptible to being eroded and carried into the S-layer by water. In contrast, less porosity and a higher proportion of fine particles in the FSC material of the S-layer. Upstream fine particles are susceptible to water erosion downstream, which causes more fine particles to accumulate in the S-layer and enhances the impermeability of the material of the S-layer in the short-term period. Consequently, higher peak water pressures occurred for experiments with a TGI of 1.25 for the U-layer. The S-layer region collapses when eroded by water due to the low proportion of

large-sized skeletal particles in the S-layer. This causes the mass of lost particles for the experiment to be larger, but the fractal dimension is smaller.

4 Conclusions

This study comprehensively investigates the mesoscopic structure and seepage characteristics of fault fracture zone with varying TGI through NMR testing, CT reconstruction, triaxial permeability test, and erosion water inrush experiments. The research explores the impact of filling gradation and zonal

filling characteristics on water inrush in fault fracture zones. The following conclusions were drawn:

(1) Porosity, proportion of macropores, connectivity of pores, coordination number, and throat equivalent radius exhibit a directly proportional relationship with TGI. As the TGI decreases from 1.25 to 0.35, the mean porosity obtained from NMR tests decreases from 16.1 to 8.28%. Additionally, the connectivity of pores decreases from 2.88 to 1.07.

(2) Filling gradation and confining pressure greatly affect the permeability of FSC materials. When the TGI was reduced from 1.25 to 0.65, the permeability of FSC material under 5 MPa confining pressure was sharply reduced from 1.3135×10^{-6} cm•s^{-1} to 0.0169×10^{-6} cm•s^{-1}, which was reduced by 98.71%. When the confining pressure was increased from 5 MPa to 15 MPa, the permeability of TGI of 1.25 decreased sharply from 1.3135×10^{-6} cm•s^{-1} to 0.5464×10^{-6} cm•s^{-1}, which was reduced by 58.4%.

(3) The water inrush process can be divided into four stages based on the time-varying curves of water pressure and flow rate: the initial impermeability stage, the rapid expansion stage of seepage channels, the steady expansion stage of gushing channels, and the stable stage of water inrush.

(4) Under equivalent LWP, the mass of the water inrush and the fractal dimension of the lost particles is directly proportional to the TGI. The duration of the initial impermeability stage, the hysteresis of water pressure transmission, the peak water pressure, and the mass of lost particles are inversely proportional to the TGI. With the same TGI, an increase in LWP causes a decrease in the duration of the initial impermeability phase, an increase in peak water pressure, and an increase in the amount of sudden water flow.

(5) As the area with larger TGI is used as the initial impermeable zone, the duration of the initial impermeable stage is shorter, and the peak water pressure, the mass of water inrush, and the mass of lost particles are greater, but the fractal dimension of the lost particles is smaller, for the same LWP. Under the conditions of the same zonal filling characteristic, the peak water pressure increases proportionally with the increase of LWP. Simultaneously, the moment of water inrush advances with the increase of LWP.

Data Availability The data that support the findings of this study are available from the corresponding author upon reasonable request.

Declarations

Ethics approval Not applicable.

Consent to publish All the authors have approved the manuscript for submission and publication.

Competing interests I would like to declare that the authors have no competing interests as defined by Springer, or other interests that might be perceived to influence the results and/or discussion reported in this paper.

References

Cai YD, Liu DM, Pan ZJ, Yao YB, Li JQ, Qiu YK (2013) Pore structure and its impact on CH4 adsorption capacity and flow capability of bituminous and subbituminous coals from Northeast China. Fuel 103:258–268. https://doi.org/10.1016/j.fuel.2012.06.055

Fan N, Wang JR, Deng CB, Fan YP, Wang TT, Guo XY (2020) Quantitative characterization of coal microstructure and visualization seepage of macropores using CT-based 3D reconstruction. J Nat Gas Sci Eng 81:103384. https://doi.org/10.1016/j.jngse.2020.103384

Gastal ESL, Oliveira MM (2012) Adaptive manifolds for real-time high-dimensional filtering. ACM Trans Graphics (TOG) 31(4):1–13. https://doi.org/10.1145/2185520.2185529

Heidary M (2021) Determination of in situ wettability using wavelet analysis and nuclear magnetic resonance log data. Nat Resour Res 30:2777–2788. https://doi.org/10.1007/s11053-021-09847-z

Hu YQ, Zhao YS, Yang D (2007) Simulation theory & method of 3D solid-liquid coupling. J Liaoning Tech University(Natural Science) 26:204–206. https://doi.org/10.3969/j.issn.1008-0562.2007.02.013

Huang Z (2016) Seepage evolution in rock masses and catastrophe mechanism of water inrush under liquid-solid coupling effect. Dissertation, China University of Mining and Technology

Huang Z, Li XZ, Li SJ, Zhao K, Xu HW, Wu R (2018) Research and development of similar material for liquid-solid coupling and its application in tunnel water-inrush model test. J Cent South University(Science Technology) 49:029–3039. https://doi.org/10.11817/j.issn.1672-7207.2018.12.017

Huang D, Huang WB, Ke CY, Song YX (2021) Experimental investigation on seepage erosion of the soil-rock interface. Bull Eng Geol Environ 80:3115–3137. https://doi.org/10.1007/s10064-021-02104-w

Huang CF, Zhang SL, Gao YT, Wu SC, Zhou Y, Sun H, Wang WQ, Wang Y, Yang WZ (2022) Triaxial permeability test of fault fractured tuff based on Talbot-theory. J Cent South University(Science Technology) 53(8):3092–3103. https://doi.org/10.11817/j.issn.1672-7207.2022.08.026

Iraj PT, Rajabi M, Ranjbar-Karami R (2023) Integrated Petrophysical and heterogeneity assessment of the karstified fahliyan formation in the abadan plain, Iran. Nat Resour Res 32:1067–1092. https://doi.org/10.1007/s11053-023-10175-7

Li Q (2018) Study on Deformation and Penetration Behavior of Crushed Rock under Shear Action. Dissertation, China University of Mining and Technology

Li SC, Song SG, Li LP, Zhang QQ, Wang K, Zhou Y, Zhang Q, Wang QH (2013) Development on subsea tunnel model test system for solid-fluid coupling and its application. Chin J Rock Mechan Eng 32:883–890. https://doi.org/10.3969/j.issn.1000-6915.2013.05.005

Li CZ, Liu GD, Cao Z, Yuan W, Wang P, You Y (2019) Analysis of petrophysical characteristics and water movability of tight sandstone using low-field nuclear magnetic resonance. Nat Resour Res 29:2547–2573. https://doi.org/10.1007/s11053-019-09582-6

Liu JF, Cao XL, Xu J, Yao QL, Ni HY (2020) A new method for threshold determination of gray image. Geomech Geophys Geo-Energy Geo Resour 6:1–13. https://doi.org/10.1007/s40948-020-00198-2

Luo P, Zhang ZY, Geng XY, Xue KS, Guang WF (2022) Evaluation of ScCO2-water performance on bituminous coal: insights from experiments and 3D CT image reconstruction. Geomech Geophys Geo-Energy Geo-Resour 8(4):118. https://doi.org/10.1007/s40948-022-00420-3

Ma D, Rezania M, Yu HS, Bai HB (2017) Variation of hydraulic properties of granular sandstones during water inrush: effect of small particle migration. Eng Geol 217:61–70. https://doi.org/10.1016/j.enggeo.2016.12.006

Markussen H, Dypvik H, Hammer E, Long HL, Hammer O (2019) 3D characterization of porosity and authigenic cementation in triassic conglomerates/arenites in the Edvard Grieg field using 3D micro-CT imaging. Mar Pet Geol 99:265–281. https://doi.org/10.1016/j.marpetgeo.2018.10.015

Ramesh S, Thyagaraj T (2022) Segmentation of X-ray tomography images of compacted soils. Geomech Geophys Geo-Energy Geo-Resour 8:1–18. https://doi.org/10.1007/s40948-021-00322-w

Scibek K, Annesley IR (2021) Permeability testing of drill core from basement rocks in the fault-hosted gryphon U deposit (Eastern Athabasca Basin, Canada): insights into fluid-rock interactions related to deposit formation and redistribution. Nat Resour Res 30(4):2909–2956. https://doi.org/10.1007/s11053-021-09811-x

Sun B, Hou SS, Zeng S, Bai X, Zhang SW, Zhang J (2020) 3D characterization of porosity and minerals of low-permeability uranium-bearing sandstone based on multi-resolution image fusion. Nucl Sci Tech 31:117–136. https://doi.org/10.1007/s41365-020-00810-w

Wang MS (2003) China has the largest amount of tunnels and underground works in the world with most complicated geological conditions and has a foreseeable quickest development in the future. Railw Stand Des. https://doi.org/10.3969/j.issn.1004-2954.2003.01.001

Wang JB (2014) 3D reconstruction of porous rock and numerical simulations of fluid flow at mesoscale levels. Dissertation, China University of Mining and Technology

Wang YC, Liu Y, Zhao N, Jiang W (2022) Investigation on the evolution mechanism of water and mud inrush Disaster in fractured rock mass of mountain tunnel. Nat Hazards Risk 13:1780–1804. https://doi.org/10.1080/19475705.2022.2082327

Wu Y (2019) Study on mechanism of unsaturated seepage of fractured sandstone based on neutron imaging. Dissertation, China University of Mining and Technology

Wu JY (2019a) Macroscopic and microscopic mechanical properties and creep model of cemented waste rock backfill. Dissertation, China University of Mining and Technology

Wu JY, Feng MM, Mao XB, Xu JM, Zhang WL, Ni XY, Han GS (2018) Particle size distribution of aggregate effects on mechanical and structural properties of cemented rockfill: experiments and modeling. Constr Build Mater 193:295–311. https://doi.org/10.1016/j.conbuildmat.2018.10.208

Wu LY, Ma D, Wang ZF, Zhang JW (2022a) Prediction and prevention of mining-induced water inrush from rock strata separation space by 3D similarity simulation testing: a case study of Yuan Zigou coal mine, China. Geomech Geophys Geo-Energy Geo-Resour 8(6):1–19. https://doi.org/10.1007/s40948-022-00518-8

Wu Y, Peng K, Zou QL, Long K, Wang YQ (2022b) Tensile properties and damage evolution laws of granite after high- and low-temperature cycles. Nat Resour Res 31:1289–1306. https://doi.org/10.1007/s11053-022-10025-y

Xie HP, Gao F, Zhou HW, Zou JP (2003) Fractal fracture and fragmentation in rocks. J Disaster Prev Mitigation Eng 23:1–9. https://doi.org/10.3969/j.issn.1672-2132.2003.04.001

Xie DS, Cai H, Wei YQ, Li WC (2015) Scaling principle and method in seepage tests on coarse materials. Chin J Geotech Eng 37(2):369–373. https://doi.org/10.11779/CJGE201502023

Yin SH, Chen X, Liu C, Wang LM, Yan RF (2020) Effects of ore size distribution on the pore structure characteristics of packed ore beds. Chin J Eng 42:972–979. https://doi.org/10.13374/j.issn2095-9389.2020.01.17.002

Yu J, Lv XB, Qin YJ (2021) Experimental study on concrete beams without web reinforcement based on fractaltheory. Chin J Eng 43:1385–1396. https://doi.org/10.13374/j.issn2095-9389.2020.03.19.003

Yu LY, Xu HB, Bai Y, Niu WQ, Tian LY, Zhang HJ (2023) CT-based 3D pore-fracture network analysis of volcanic reservoirs of lower cretaceous yingcheng formation in southern Songliao Basin, China: impact on natural gas migration. Geoenergy Sci Eng 223:211581. https://doi.org/10.1016/j.geoen.2023.211581

Zhang R (2014) Activation seepage mechanism on structural fracture zone of coal seam floor in mining above aquifer. Dissertation, China University of Mining and Technology

Zhang R, Ai T, Li HG, Zhang ZT, Liu JF (2013) 3D reconstruction method and connectivity rules of fracture networks generated under different mining layouts. Int J Min Sci Technol 23:863–871. https://doi.org/10.1016/j.ijmst.2013.10.013

Zhang TJ, Pang MK, Peng WQ, Liu N, Huang YG (2019) Seepage stability of cemented and fractured coal rock mass under tri-axial stress. J Min Saf Eng 36(04):834–840. https://doi.org/10.13545/j.cnki.jmse.2019.04.024

Zhang QY, Chen WZ, Yuan JQ, Liu Q, Rong C (2020) Experimental study on evolution characteristics of water and mud inrush in fault fractured zone. Rock Soil Mech 41:1911–1922. https://doi.org/10.16285/j.rsm.2019.1527

Zhang GQ, Chen Y, Lu HB, Li XF (2022a) Fractal characteristics of fiber lithium slag concrete cracks under sulfate Attack. Chin J Eng 44:208–216. https://doi.org/10.13374/j.issn2095-9389.2020.09.10.001

Zhang GT, Chen Y, Lu HB, Li XF (2022b) Fractal characteristics of fiber lithium slag concrete cracks under sulfate Attack. Chin J Eng 44(2):208–216. https://doi.org/10.13374/j.issn2095-9389.2020.09.10.001

Zhou Y, Li SC, Li LP, Zhang QQ, Shi SS, Song SG, Wang K, Chen DY, Sun SQ (2015) New technology for fluid-solid coupling tests of underground engineering and its application in experimental simulation of water inrush in filled-type karst conduit. Chin J Geotech Eng 37:1232–1240. https://doi.org/10.11779/CJGE201507009

Zhou G, Zhang Q, Bai RN, Ni GH (2018) Minerals characterization of coal micro-pore structure and simulation on the seepage rules of low-pressure water based on ct scanning data. Minerals 6:78. https://doi.org/10.3390/min6030078

Zhu C, Wang YM, Weng HY (2011) Study of scale effect of coarse-garined DAM materials. Chin J Rock Mechan Eng 30:348–357